PNAS RESEARCH ARTICLE | BIOPHYSICS AND COMPUTATIONAL BIOLOGY

Structure of an amorphous calcium carbonate phase involved in the formation of *Pinctada margaritifera* shells

Tilman A. Grünewald[a,1,2], Stefano Checchia[b,1], Hamadou Dicko[a], Gilles Le Moullac[c], Manaarii Sham Koua[c], Jeremie Vidal-Dupiol[d], Julien Duboisset[a], Julius Nouet[e], Olivier Grauby[f], Marco Di Michiel[b], and Virginie Chamard[a]

Edited by Pupa Gilbert, University of Wisconsin–Madison, Madison, WI; received July 22, 2022; accepted October 3, 2022 by Editorial Board Member Joanna Aizenberg

Some mollusc shells are formed from an amorphous calcium carbonate (ACC) compound, which further transforms into a crystalline material. The transformation mechanism is not fully understood but is however crucial to develop bioinspired synthetic biomineralization strategies or accurate marine biomineral proxies for geoscience. The difficulty arises from the simultaneous presence of crystalline and amorphous compounds in the shell, which complicates the selective experimental characterization of the amorphous fraction. Here, we use nanobeam X-ray total scattering together with an approach to separate crystalline and amorphous scattering contributions to obtain the spatially resolved atomic pair distribution function (PDF). We resolve three distinct amorphous calcium carbonate compounds, present in the shell of *Pinctada margaritifera* and attributed to: interprismatic periostracum, young mineralizing units, and mature mineralizing units. From this, we extract accurate bond parameters by reverse Monte Carlo (RMC) modeling of the PDF. This shows that the three amorphous compounds differ mostly in their Ca–O nearest-neighbor atom pair distance. Further characterization with conventional spectroscopic techniques unveils the presence of Mg in the shell and shows Mg–calcite in the final, crystallized shell. In line with recent literature, we propose that the amorphous-to-crystal transition is mediated by the presence of Mg. The transition occurs through the decomposition of the initial Mg-rich precursor into a second Mg-poor ACC compound before forming a crystal.

biomineralization | nonclassical crystallization | calcium carbonate | amorphous calcium carbonate

Significance

The formation mechanism of calcareous biominerals is a topic of intense research. In recent years, the importance of amorphous calcium carbonate precursors in their formation has been recognized, but until now, a quantitative characterization of the possible different amorphous compounds in the mineralizing organism is lacking. The character of the amorphous calcium carbonate compounds is a critical factor for the understanding of the initial stages of the mineralization process and the underlying crystallization pathway. We show by nanobeam X-ray total scattering analysis three distinct amorphous calcium carbonate phases, differing in their bond structure, are present in the early mineralization stages of the oyster *Pinctada margaritifera*. This allows us to propose an amorphous to crystallization scheme for its prismatic layer.

Species over all five biological kingdoms employ biomineralization as an answer to specific problems (1). This central constituent of the physiological activities is remarkable: It relies on different mineralization strategies exerted by the living organisms and results in a variety of hard tissue morphologies, involving different mineral compounds and various crystalline and amorphous polymorphs (1). However, an overarching nanoscale organo-mineral motif referred to as granules, observed for many species and orders (2–4) with occurrences dating back to the Ediacaran period (5), points toward generic mechanisms in the biomineralization process. Understanding these mechanisms is a challenge of utmost importance as it might be the key to develop bio-inspired mineralization strategies for tough and gossamer ceramics (6) or hierarchical structures (7). In paleoclimatology, where marine biomineral proxies are used as paleotracers, understanding the biomineralization mechanisms is a key factor for improving the accuracy of thermal records (8).

For most crystalline biominerals, the granular organization (9) associated with crystallization kinetics, which involves different mineral polymorphs (10, 11), points toward a mechanism different from classical crystallization theory (defined as the addition of individual ions or molecules from a solution to a final bulk crystal). The complexity of this question—the description of the biomineralization pathways—is illustrated by the different aspects one has to address to fully understand and ultimately reproduce the biomineralization mechanisms. From a physicochemical point of view, it requires identifying the different minerals and organic molecules at play during the mineralization process. Moreover, it also necessitates characterizing the morphology of these constituents, the successively appearing polymorph phases, and the nature of the different phase transitions. While the detailed descriptions of the final biominerals are widely documented, the characterization of the transient states is challenging, as most of the experimental approaches are performed ex vivo (11, 12).

In calcium carbonate biominerals, the repeated presence of an amorphous calcium carbonate (ACC) phase, an otherwise metastable $CaCO_3$ polymorph reported in sea echinoderms (11), molluscs (13–18), and crustaceans (19, 20), is regarded as a transient precursor of the crystallization pathway (21), which could be temporarily stabilized by

Author contributions: T.A.G. and V.C. designed research; T.A.G., H.D., G.L.M., M.S.K., J.D., J.N., O.G., and M.D.M. performed research; S.C. and J.V.-D. contributed new reagents/analytic tools; T.A.G., S.C., and V.C. analyzed data; and T.A.G. and V.C. wrote the paper.

The authors declare no competing interest.

This article is a PNAS Direct Submission. P.U.P.A.G. is a guest editor invited by the Editorial Board.

[1]T.A.G. and S.C. contributed equally to this work.

[2]To whom correspondence may be addressed. Email: tilman.grunewald@fresnel.fr.

This article contains supporting information online at http://www.pnas.org/lookup/suppl/doi:10.1073/pnas.2212616119/-/DCSupplemental.

Published November 2, 2022.

factors such as granules of finite size (22, 23), organic macromolecules (21) or trace elements (e.g., Mg) (21, 24), and/or by the mantle cells (25). The presence of ACC is often observed, indicating its involvement in the crystallization and justifying this question as a topic of intensive research. It includes its speciation and the possible presence of multiple amorphous phases, referred to as polyamorphism (26, 27) and defined herein as different atomic structures at short length scale (1 to 5 Å). In synthetic systems, the existence of distinct, different ACC phases could be demonstrated, which in turn also crystallize into different crystal structures (28, 29). The amorphous phases are identified based on their local (i.e., short range) structure, which resembles their final crystallized form (i.e., aragonite, vaterite, and calcite in the mentioned studies). The crystalline polymorph can be tuned by changing the pH level (28) or the polymeric compounds during the early stages of ACC formation (30), resulting in different amorphous species of varying solubilities, affecting their thermodynamic stability (31). While the synthetic compounds readily crystallize from the amorphous state, ACC in biominerals shows remarkable stability and is even present in the final, crystallized biomineral, which helps to deduce its chemical nature. Moreover, there is evidence that compositional differences could also play a role in the formation of biominerals. Recent research showed the presence of hydrated and anhydrous ACC in corals (32), sea urchin spines (11, 33, 34), or the nacreous layer of bivalves (35) by X-ray photo emission spectroscopy. However, it is not clear whether polyamorphism is at play here. The coexistence of amorphous and crystalline phases in spatial proximity led to the hypothesis of a transformation via secondary nucleation onto an existing crystalline layer (10, 11). In this scenario, the mineralization proceeds in three steps: i) the formation of hydrated ACC, which transforms quickly into ii) an instable anhydrous form, which finally transforms into iii) calcite.

Further identification of the transient amorphous phases in biogenic systems requires highly sensitive and highly spatially resolved spectroscopic techniques. Commonly used vibrational spectroscopy techniques like Fourier-transform infrared spectroscopy (36) and Raman scattering (37, 38) offer excellent sensitivity for specific bonds and add important insights into the accessible bonds. They are however not perfectly suited to resolve the finer details of the bond structure. Other techniques like X-ray absorption near-edge structure (39) and X-ray photo emission spectroscopy (40, 41) are sensitive to the very local environment of a target atom and are extremely useful for the case where known reference substances are available (42). By studying the extended X-ray absorption fine structure, the short- and medium-range order can be determined, but it requires scanning a wide energy range of ~2 keV. Thus, attaining spatial resolution with a tightly focused X-ray beam renders the X-ray spectroscopic approach difficult due to the energy-dependent beam movement onto the sample. Furthermore, the available absorption edges are limited by the accessible energy range of the instrument and by sample attenuation and self-absorption considerations. Finally, spectroscopic-ptychography approaches allow the circumvention of the necessity of a tightly focused X-ray beam, but the acquisition of spectra with high signal-to-noise ratio requires extended experimental sessions (43–46). Furthermore, they are usually carried out in the near-edge regime (43–46), which does not yield quantitative information on the short- and medium-range bond structures. While these techniques have generated a great deal of insights, alternative strategies are needed in addition to improve our understanding of the structure of the amorphous phases.

An alternative strategy relies on the investigation of the pair distribution function (PDF), i.e., the distribution of atom pair distances contained in a given volume. This is usually obtained from the measurement of the two-dimensional (2D) (diffuse) scattering signal produced by the amorphous phase from neutron or X-ray scattering, which is used to further extract the PDF by Fourier transformation. This approach has already been successfully applied to study "medium-range" structures (from 5 up to 15 Å) in pure synthetic ACC (47–49). While this technique has found widespread application in the study of bulk amorphous systems (50, 51) and bulk biominerals (33, 52), recent progress in synchrotron hard X-ray instrumentation has brought spatially resolved (below 1 μm) PDF within reach. Since full spectral information is acquired in a single 2D diffraction pattern in a very short time, PDF has become a viable option to characterize samples with high spatial resolution. This method has been applied to hard condensed matter problems such as state of matter under extreme conditions with microfocused X-ray beams (53), structural organization in thin films via grazing incidence PDF (54), or even three-dimensional studies by using PDF tomography (55). So far, the application to biominerals has been hampered by the low scattering power of the amorphous compounds and the parasitic contribution of the crystalline phase. These two difficulties have been overcome in the present study by gathering a larger portion of the reciprocal space and using a filtering approach to eliminate the parasitic crystalline contributions. The obtained PDF signal can be analyzed with standard analytical tools such as principal component analysis (PCA) (56, 57) and reverse Monte Carlo (RMC) modeling (27, 48, 49, 58) to gain new insights into the structure and distribution of the amorphous compounds. For reasons of brevity, we refer the reader to *Materials and Methods* for further details on the data analysis approach.

Using submicrometer resolved PDF analysis, we show how one can extract the amorphous contribution from calcareous crystallized mineralizing units of a juvenile *P. margaritifera* mollusc shell and use it for structural characterization of ACC at the atomistic level. Our spatially resolved analysis identified three main amorphous contributions, one arising from the organics and another two from the mineral phase, apparently related to the aging of the mineralizing unit. Finally, a reverse Monte Carlo data modeling approach was used to obtain characteristic atom pair distances in the amorphous phase. In addition, spectroscopy results based on coherent Raman microscopy and energy dispersive X-ray microscopy evidenced the presence of Mg-rich calcite and Mg atoms with a specific spatial distribution. This complementary set of results led us to propose a Mg-mediated mechanism by which the amorphous phase transforms into calcite in this system, forming the basis for studies of the amorphous components in further biomineralizing systems.

Results

Juvenile *P. margaritifera* specimens were chosen for the morphology of their calcareous shell (Fig. 1*A*), which allows easy access to preserved early mineralizing crystalline units and allows us to selectively probe the early stages of mineralization. Each valve of the shell is organized in two main mineralized layers: an external layer composed of elongated calcite prisms and an inner layer made of aragonitic nacreous tablets (59). The outside of the shell is lined with a thin organic membrane, the periostracum, and both prisms and nacre tablets are enveloped in thin organic sheaths (16, 60). While all these organic layers are composed of proteins, sugars, and lipids (16, 61), the prismatic layer is produced by cells located at the very edge of

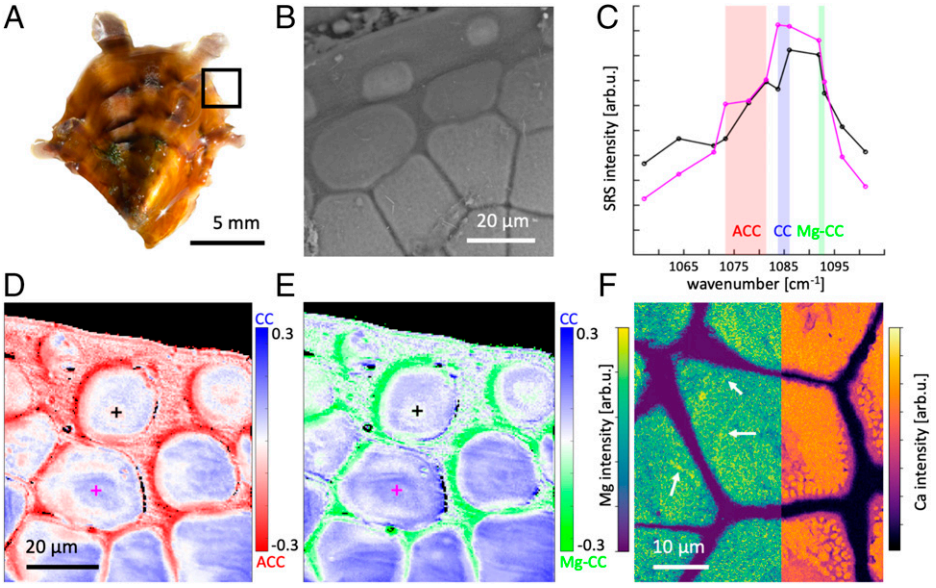

Fig. 1. Structure and composition of *P. margaritifera* shells. (*A*) Micrograph of a juvenile *P. margaritifera* specimen. The black rectangle indicates the investigated shell edge. (*B*) SEM image of the shell edge, showing the isolated, disc-like early mineralization units at the *Top* and the more developed prism structure that is slowly forming. (*C*) SRS spectrum (bulk sensitive) of an early (black) and more mature (magenta) region of the shell, exhibiting spectral features of ACC (red region), CC (blue region), and Mg–CC (green region). The location of the two spectra is indicated by crosses in *D* and *E*. (*D*) Symmetric contrast map of ACC (red) vs. CC (blue), showing the presence of ACC, in particular in the early stage discs as well as an accumulation of ACC around the discs and prisms. Black and magenta crosses indicate the position of the spectra shown in *C*. (*E*) Symmetric contrast map of Mg–calcite (green) vs. CC (blue). The maps show the presence of Mg–calcite in the sample, in particular in the early-stage discs but also strongly around discs and in interprismatic units. (*F*) EDX map (surface sensitive) displaying the qualitative distribution of Mg and Ca in a mature prism. The Mg map shows the presence of Mg in the prism. Interestingly, we observed repeatedly annular structure of higher Mg content in the prisms (highlighted with white arrows). The Ca signal shows rather homogenous distribution of Ca throughout the sample, with a slight depletion in the center of the prism and a heterogeneous distribution toward the prism edges.

the animal mantle and the nacre layer by other, more internal cells (62). Therefore, only the prismatic layer is present at the shell edge (Fig. 1*B*). In the mature part of the prismatic layer, the prisms are juxtaposed polygonal units with a typical size of 20 to 50 µm. In their early stages of mineralization, they are isolated, thin disc-like units (59), visible at the very edge of the shell. The isolation greatly facilitates the experimental characterization, and a further characterization of their structure is presented by Duboisset et al. (12). The discs grow freely until their expansion is constrained by neighboring units. Investigation of the growth edge with stimulated Raman spectroscopy (SRS), a coherent Raman spectromicroscopy approach, allows us to visualize the distribution of chemical structures within the sample by targeting specific chemical bond vibrations. Here, for our spectral analysis we have chosen three distinct spectral regions, indicated as colored regions in Fig. 1*C*. We chose the crystalline calcite (CC) symmetric C–O stretch (ν_1) at 1,085 cm^{-1} (63) (blue-shaded region in Fig. 1*C*), the previously reported biogenic amorphous $CaCO_3$ (ACC) vibrations, a broad (30 cm^{-1}) peak at about 1,080 ± 5 cm^{-1} (64) (red-shaded region in Fig. 1*C*), and the symmetric C–O stretch (ν_1) of Mg–calcite (Mg–CC) at about 1,093 cm^{-1} (37) (green-shaded region in Fig. 1*C*). Two example spectra are shown from a younger disc (black line, position marked by black cross in Fig. 1 *D* and *E*) and a more mature prismatic unit (magenta line, position marked by magenta cross in Fig. 1 *D* and *E*). We chose to average a slightly larger spectral range around each target vibration (see colored regions in Fig. 1*C* and *Materials and Methods* for more detail) to account for observed fluctuations in the peak position, potentially arising from local compositional fluctuations. The resulting individual intensity maps are presented in *SI Appendix*, Fig. 1. While the spectral resolution of the SRS approach (~12 cm^{-1}) does not enable an absolute quantification of the different constituents (e.g., the ACC signal still contains a contribution from CC excited by the higher wavenumber tails of incidents beams), we were able to eliminate the effect of parasitic signals by calculating the symmetric difference of the intensity maps, i.e., the difference between the CC and ACC (respectively [resp.] CC and Mg–CC) intensity images, normalized by the sum of the two maps. In this way we produced divergent distribution maps (Fig. 1 *D* and *E*), where higher values correspond to CC-rich regions and lower values to ACC-rich or Mg–CC-rich regions; the individual intensity maps are presented in *SI Appendix*, Fig. 1. A more detailed account and simulations are presented in ref. 12. Fig. 1*D* shows the distribution of CC-rich (blue) and ACC-rich (red) regions. While the more mature prisms at the bottom exhibit a CC-dominated signal, the younger discs exhibit elevated levels of ACC-rich signal, especially in their center, along annular structures (rings) and at their margins. Fig. 1*E* displays the distribution of CC (blue) and Mg–CC (green) contrast. The Mg–CC distribution pattern is largely similar to ACC, indicating that the ACC-rich and Mg–calcite-rich signals are found in the same regions of the sample: the early discs, the rings, and their margins. To quantify the amount of Mg in the Mg–CC phase more accurately, we have carried out micro-Raman spectroscopy experiments. Thanks to the largely enhanced spectral resolution of this method, the ACC, CC, and Mg–CC contributions to the ν_1 peak can be accurately deconvoluted; and therefore, from the Mg–CC peak position and the known peak shift relation, we can determine the ratio of Mg to Ca in the Mg–CC contribution (65). The results are presented in *SI Appendix*, Fig. 2 *B–D* and the full fit results are presented in *SI Appendix*, Fig. 3. The Mg–CC content in early-stage discs (9.77% ± 2.43) is significantly higher compared to mature prisms (8.77% ± 2.99). An additional observation is the comparable peak width of the CC and Mg–CC contribution (5 to 10 cm^{-1}), which is indicative of a crystalline contribution rather than the broad width of 20 cm^{-1} or more, which an amorphous compound would

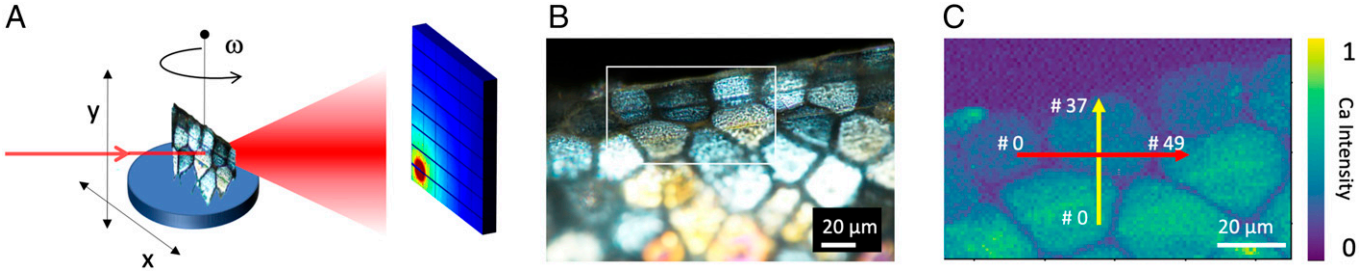

Fig. 2. PDF data acquisition and sample. (*A*) PDF nanobeam (500-nm width) scanning setup showing the sample translation in *x*-*y* and the rotation around ω. The scattered radiation (red cone), including diffuse scattering and crystalline Bragg peaks, was collected by a 2D detector. (*B*) The optical wide field image shows the presence of early-stage discs and more mature prisms in the selected sample. The region in the blue rectangle was further investigated in *C*. An XRF map of the Ca K_α fluorescence, showing the early-stage disc and its neighboring discs and prisms. Horizontal (red line) and vertical (yellow line) line scans were carried out with a 1-µm step size. The start/stop scan positions are indicated in the scan.

produce. Consequently, evidencing the presence of different ACCs (weak contribution and large peak width) is here rather challenging and likely beyond the limit of the two considered Raman approaches. In order to track the elemental composition, energy-dispersive X-ray spectroscopy (EDX) was used to map the Ca and Mg distribution in the sample (Fig. 1*F*). The Mg map shows the presence of Mg in the prisms, in particular, distributed over several annular zones. The Ca map shows rather homogeneous regions alternated with depletion regions in the center of the prism, while the outer margins exhibit a heterogeneous distribution structure. In addition to the data from a single sample we present here, these observations were confirmed through the investigation of 10 other samples, which exhibit consistent behavior with respect to our previous work (12).

While SRS and EDX are powerful tools to map out chemical and elemental species with high sensitivity and spatial resolution, information on the fine structure of the (possibly different) amorphous compounds is better attained through the PDF approach presented below. Recent improvements in high-energy X-ray instrumentation, like the availability of submicrometric beams (66) and the advent of hard X-ray single photon counting detectors (67, 68), provide the improved spectral resolution, weak-signal sensitivity, and spatial resolution that enable nano-resolved PDF analysis. In addition, to isolate the amorphous contribution from the crystallized mineralized prismatic units, we designed the data acquisition and analysis strategy described hereafter.

Fig. 2*A* shows a scheme of the synchrotron-based PDF setup, where the sample scanning directions, along *x* and *y*, allow one to translate the sample across the incoming beam (500-nm width). An additional scanning rotation, named ω, allows the rotation of the sample about the vertical axis. The illumination of the sample by a high-energy X-ray beam (60 keV) results in diffracted and diffuse scattering intensity patterns reaching the 2D detector placed perpendicular to the forward beam direction. By acquiring the intensity patterns over a 30° range of tilt angle about the vertical axis (ω), it is possible to explore a large portion of the reciprocal space for each individual position along *x* and *y*. The single-crystalline regions of the biomaterial gives rise to Bragg peaks appearing as sharp, isolated signals both on the detector and along the angular scan, while the scattering contribution from the amorphous compounds in the sample is invariant along the ω-rotation direction. Low-pass filters applied to the scattering intensities sorted along the rocking axis ω provides an efficient means to separate the crystalline scattering contribution from the amorphous, and therefore retain only the latter component for subsequent PDF analysis (*SI Appendix*, Fig. 4). Prior to the diffraction experiment, the shell border was surveyed visually (Fig. 2*B*) with crossed-polarized light microscopy. Having thus determined the morphology of the shell border, the X-ray fluorescence (XRF) signal of Ca was then used at the synchrotron beamline to select a region of interest for diffraction scans (Fig. 2*C*). Finally, two datasets were acquired along *x*, *y* line scans (red and yellow lines in Fig. 2*C*), using a 1-µm step size. The lines cover an early-stage disc as well as more mature neighbor prisms, further away from the growth edge.

The extracted experimental scattering data *I(q)*, with *q* being the amplitude of the scattering vector (Fig. 3*A*), is reduced to the structure function *S(q)* (Fig. 3*B*) and then further transformed into the pair-distribution function, *D(r)* with *r* being the distance between atoms (further described in *Materials and Methods* as well as in *SI Appendix*, Fig. 5). The presence of resolved maxima in *D(r)* provides direct access to the characteristic interatomic distances in the sample representing short-range order (1 to 5 Å). The lack of a long-range ordered structure in the amorphous compound thus isolated is visible in the rapid intensity falloff of *D(r)* as well as the featureless *I(q)* and *S(q)* function (Fig. 3 *A* and *C*).

In order to extract some characteristic components of the PDF, a PCA was first performed, using non-negative matrix factorization (*Materials and Methods*) on the normalized function $G'(r)$ (Fig. 4*A*), where the different peak contributions have been numbered from #1 to #5. These features are located at 2.35 Å (#1), 2.8 Å (#2), 3.2 Å (#3), 3.7 Å (#4), and 4.3 Å (#5) and match well with reported values in the literature, summarized in *SI Appendix*, Tables 1 and 2. We stress here that, since each PDF feature can reflect multiple, overlapping sets of interatomic distances, the PCA approach is motivated by its independence of peak assignments. To ensure consistency in the analysis, the three principal components (labeled PC1, PC2, and PC3) of the decomposition (shown in Fig. 4*A*) were kept constant for the two line scans, while their respective contributions were adjusted to fit the data. In total, the three first principal components (PCs) account for more than 96% of the variability of the dataset (*SI Appendix*, Fig. 6 *A* and *B*). The very good agreement between the fit result and the data is further illustrated in Fig. 4*B* for the horizontal line scan, while the vertical line scan is presented in *SI Appendix*, Fig. 6*C*. The three PCs look appreciably different and combine to match closely the overall shape of the PDF. The most visible feature is a shift of peak #1. It shows a strong shift in PC2 to smaller distances compared to PC1 and PC3. The peaks #2, #3, and #4 are distributed among the three PCs with shifts in their position, while peak #5 appears only in PC2. While the PCs retrieved are not necessarily representing individual components in a 1:1 fashion, we note that their shape bears resemblance to the PDF of different amorphous compounds. PC1 reproduces the prominent peaks #1, #3, and #4, which were reported in the *G(r)* of ACC (27, 48, 69). PC2 with its shift of peak #1 resembles the

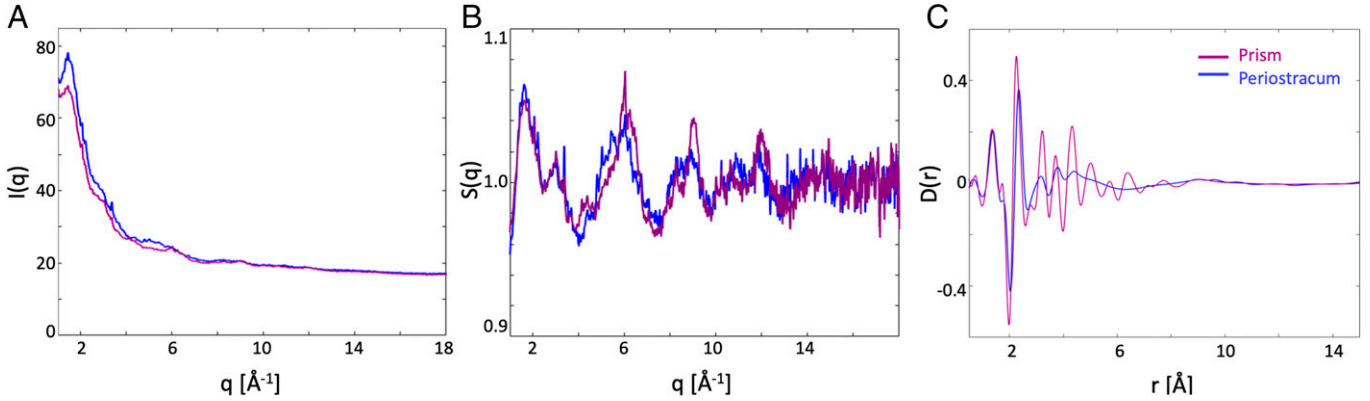

Fig. 3. Total scattering data after removing the crystalline contribution. (*A*) Scattered intensity summed over five scan positions for a horizontal line position in the periostracum (from positions #9 to #14, blue) and the prism (from #31 to #35, purple), exhibiting diffuse scattering features at about 2.5, 5, and 9 $Å^{-1}$. (*B*) The structure function *S(q)*, obtained after removing the atomic form factor contribution, highlights the oscillations due to the sample structure. (*C*) The pair distribution function *D(r)* obtained after data treatment and Fourier transformation, giving insights into the local atomic distribution structure.

G(r) of amorphous magnesium carbonate, which features peaks at ~2.1 Å and 3.8 Å (70, 71). PC3 bears some characteristics of ACC *G(r)* (27, 48, 69) again, in particular peak #2 at 2.8 Å, which was not featured in PC1.

The relative contributions of the PCs are shown in Fig. 4 *C* and *D*, for the horizontal and vertical scans, respectively. From the spatial distribution of the PCs, the center of the disc presents mostly PC1 and PC2 contributions, but less PC3. The interprismatic spaces of the periostracum (visible in the horizontal line scans and highlighted by red lines) feature mostly PC1. As the prisms are tightly abutting vertically, the gap between the two mineralizing units is hardly visible, in contrast to the horizontal line, where the gap is larger and therefore, the effect appears stronger. The more mature prisms (Fig. 4 *C*, *Right* and Fig. 4 *D*, *Left*) in turn exhibit strong contributions from PC3, less PC1, and very little PC2. The two line scans are consistent with each other as they exhibit similar PC fractions at their crossing point (Fig. 4*C*, position #27 and Fig. 4*D*, position #21).

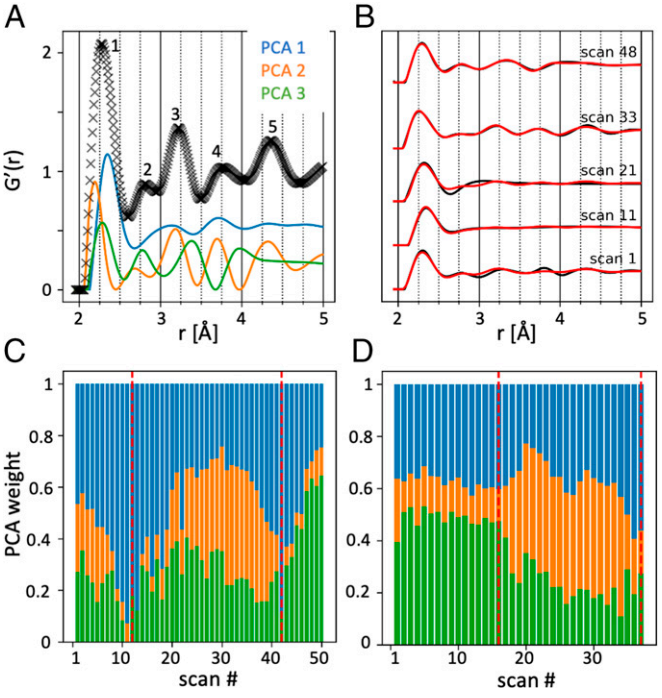

Fig. 4. Principal component analysis. (*A*) *G'(r)* of an individual scan position (black) with the respective contributions of PC1 (blue), PC2 (orange), and PC3 (green). The numbers indentify the main peaks. (*B*) Comparison of the PCA component (red) and the experimental data (black) in some positions of the horizontal line scan. (*C*) The relative contribution of the three components in each point of the horizonal line scan. The disc borders are schematically indicated by the red lines. (*D*) Same as *C*, for the vertical line scan.

While this approach helps to unravel the defining traits and relative amounts of the different contributions to the *D(r)* without prior assumptions, the chemical nature of the signal can only be inferred from comparison to reference PDF data, if available. In addition, since each component does not have to represent directly the partial PDF of a distinct phase, it is difficult to pin down the characteristic atom pair distances of each possible ACC compound by PCA alone. In order to overcome this, fitting of *D(r)* with a reverse Monte Carlo (RMC) simulation was carried out. This method calculates the scattering from an assembly of atoms whose positions are moved by small random amounts until they match the experimental data. In this way, information on the local structure and their short- and medium-range order can be obtained. It is an established tool (47, 48, 58), which allows one to study quantitative changes in the atomic arrangement of the sample. In order to check the convergence properties, every dataset was fitted four times with different, randomized starting guesses. These four runs converged to essentially similar results. The obtained structural model is shown in *SI Appendix*, Fig. 7. In *SI Appendix*, Fig. 7*A*, the $CaCO_3$ atom clusters are shown as a turquoise isosurface and the water O atoms are shown as gray spheres. This representation shows that the $CaCO_3$ clusters show a continuous, random network with the water O atoms organized around it without apparent structuring. A comparision of a typical configuration extracted from the center of the reconstructed volume is shown in *SI Appendix*, Fig. 7 *B* and *C* for a young prism (horizontal #31) and a mature prism (horizontal #48), respectively. The Ca atoms are represented as blue spheres, surrounded by their coordination of C and O atoms (brown and red spheres) together with the oxygen atoms from the water molecules (gray spheres). The configuration of the Ca atoms shows a remarkable stability between young disc and mature prism and only the coordinating C and O atoms of the carbonate group show a slightly different configuration along with the water oxygen atoms. While the atomic configuration gives an excellent insight into the structure, a more detailed analysis of the bond configuration allows a statistically more relevant analysis. We focused our analysis on the range from 2 to 4 Å, which describes the most relevant interatomic distances, i.e., those involving Ca, C, and O atoms in our sample.

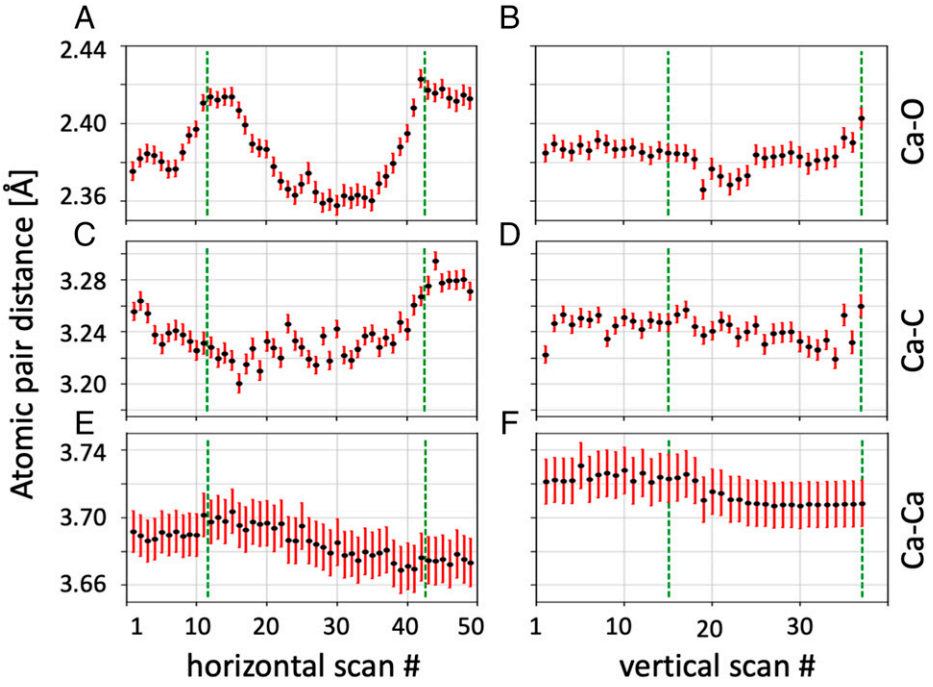

Fig. 5. Bond parameters extracted from RMC modeling. (*A*) Ca–O atom pair, horizontal line. (*B*) Ca–O atom pair, vertical line. (*C*) Ca–C atom pair, horizontal line. (*D*) Ca–C atom pair, vertical line. (*E*) Ca–Ca atom pair, horizontal line. (*F*) Ca–Ca atom pair, vertical line. Error bars show the 3σ SE.

Fig. 5 shows the bond parameters extracted from RMC modeling as a function of scan position in the horizontal (*Left* column) and vertical (*Right* column) direction, with error bars indicating the 99.7% confidence interval. The average Ca–O atom pair distance (Fig. 5*A*) shows an expansion at the edges of the disc and into more mature prisms (*Right* side of *A*), reaching 2.43 Å, whereas the atom pair distance is reduced to about 2.38 Å and 2.41 Å in the center of the disc and in the older prism, respectively. A similar behavior can be observed for the vertical line scan (Fig. 5*B*) with a reduced Ca–O atom pair distance in the disc and an increased atom pair distance in the more mature prism (first ∼15 scan positions). The Ca–C pair in the horizontal and vertical lines (Fig. 5 *C* and *D*) presents a rather similar trend with longer distances (∼3.275 Å) in the mature prism and a contraction toward the disc (∼3.23 Å). The Ca–Ca distance extracted from the horizontal line (Fig. 5*E*) is marginally shorter in the mature prism (3.65 Å) than in the center of the disc (3.66 Å). We note that the vertical line (Fig. 5*F*) shows an opposite trend with a distance slightly longer in the mature prism than the disc, probably indicating the limit of the analysis sensitivity.

Discussion

Summary of the Findings. Our SRS results show the presence of ACC in the shell structure of *P. margaritifera* and an enhanced concentration of ACC in young discs. This goes along with the specific distribution of Mg–calcite-rich regions, where both ACC-rich and Mg–calcite-rich regions are confined to annular structures and margins of mineralizing units. The investigation of a mature prism with EDX confirms the presence of Mg and unveils enrichment in annular zones, corresponding to the edges of the successive growth units as shown recently (12). PDF analysis revealed a clear spatial pattern in the structure of the ACC. The PCA decomposition, a model-free approach, shows three distinct, spatially separated PCs. PC1 is associated with the periostracum, whereas PC2 is mostly found in the younger disc and PC3 in the older prisms. The first interatomic distance of the PC2 (prevalently Ca–O) is markedly shifted toward smaller distances with respect to PC1 and PC3, with a structure resembling the *G(r)* of ACC (27, 48, 69) and amorphous magnesium carbonate (70, 71). The RMC modeling approach allowed us to model explicitly interatomic distances for the Ca–O, Ca–C, and Ca–Ca pairs. They present a consistent behavior between the two scans but also some key spatial variations. The average Ca–O distance of ∼2.4 Å is clearly different from the bond length found in crystalline calcite (2.36 Å, see *SI Appendix*, Table 3) and compares well with the literature reports of biogenic (*SI Appendix*, Table 1) and synthetic (*SI Appendix*, Table 2) amorphous calcium carbonate. The most striking feature is the contraction of the Ca–O bond in the young disc region (2.38 Å) with respect to the periostracum (2.43 Å) and the older prisms (2.41 Å), as anticipated by PCA decomposition. The clear difference in nearest-neighbor Ca–O and Ca–C distances between the young disc and older prism indicates a degree of transformation between these two amorphous components. To this regard, we note that this behavior can be explained by varying amounts of Mg in the ACC structure and does not necessarily support the notion of polyamorphism as the structures appear very similar except for their Ca–O and Ca–C distances.

Potential Amorphous Calcium Carbonate Transformation Pathways. The literature is proposing essentially two different mechanisms of amorphous calcium carbonate transformation: one invoking the presence of Mg (24, 72–74), the other a form of ACC hydration (10, 35). In brief, the first scenario involves an Mg-rich ACC phase transforming upon loss of Mg into a Mg-poor ACC (72). Although the exact composition of this phase is not clear, on an atomistic level a gradual transition between a shorter Mg–O and a longer Ca–O atom pair distance in a pure amorphous $MgCO_3$ and a pure amorphous $CaCO_3$ has been reported experimentally (75) and further confirmed by simulations (76) (see *SI Appendix*, Tables 1 and 2 for

a further summary). This is consistent with the reported Mg–O atom pair distance of a pure biogenic amorphous $MgCO_3$ carbonate of around 2.05 Å (24). We note, however, that Albéric et al. (77), reported a longer, albeit only minor (0.02 Å) difference in the bond length of fully hydrated, amorphous $MgCO_3$ with respect to the fully hydrated ACC, both being characterized in ref. 77. This contrasts with the literature cited above (24, 75, 76), with the well-reported Ca–O atom pair distance contraction if Mg is introduced into the calcite lattice (78) or with the generally smaller Mg–O bond found in Mg carbonates like dolomite or magnesite (79). A second proposed scenario focuses on the role of water, which has proved to be an alternative means of stabilizing ACC (80). There, the loss of first free and then bound water results in the formation of an anhydrous ACC phase (80). From the available data in the literature, the fully hydrated ACC phase presents a Ca–O atom pair distance longer than the semihydrated or the anhydrous phase (77, 81). We furthermore note that the anhydrous state is rather unstable due to the increased ordering upon dehydration (82–84) but is a necessary step for crystallization and might explain the repeated observation of this state during the crystallization process (80, 83). While these two scenarios present rather distinct cases of ACC stabilization and crystallization, one needs to consider the multifaceted nature of biomineralization, so some significant overlap may exist between the two scenarios as highlighted in a recent review (85). Indeed, mixed modes of Mg- and H_2O-mediated ACC stabilization exist (76). Mg ions may modify the amount of water in the ACC structure (76) and organic impurities are susceptible to stabilize differently depending on their mode of interaction (86). An additional factor influencing the short-range order is carbonate concentration at the time of formation. It was shown by Mergelsberg et al. (87) that a high carbonate ion concentration stabilizes a Ca-rich ACC phase, exhibiting a highly ordered Ca–O distance of 2.36 Å. A low carbonate ion concentration favors a Mg-rich phase with a mixed Ca and Mg short-range order. The Mg short-range order is characterized by a Mg–O distance of ∼2.13 Å.

Evidence for a Mg-Mediated Transformation Pathway. Our experimental findings point toward the Mg-stabilized ACC scenario (24, 75, 76) of a shorter Ca–O atom pair distance in the younger disc via RMC modeling; the distinct amorphous compounds in the old prisms and young disc found by PCA decomposition; the presence of Mg–calcite in the final, crystallized state by SRS microscopy and Raman microscopy; and the finding of annular zones of Mg enrichment observed by scanning electron microscopy (SEM)-EDX. Interestingly, the Mg-stabilization mechanism has been investigated in more detail recently. It was invoked to explain the formation of a prestressed biogenic calcite single crystal by the brittle star *Ophiocoma wendtii* (72) and was recently shown to be a widespread strategy of biomineralization (74). In this model, an initial Mg-rich ACC precursor undergoes a spinodal decomposition into Mg-rich amorphous nanoparticles and a Mg-depleted amorphous matrix. In a second step, these two constituents crystallize and form a biphasic structure (73). Ref. 72 also showed that, depending on the size of the Mg-rich particles, either a transportation along the crystallization front (leading to a layered structure) or direct inclusion (leading to a homogenous matrix) can be observed, based on the physical behavior of the amorphous matrix like its viscosity and the size of the Mg-rich particles. Here, the observation of 1) shorter Ca–O atom pair distance in the young disc (Fig. 5), where we expect to find fresh Mg-stabilized ACC; as well as 2) the occurrence of Mg-enriched, annular zones (Fig. 1*F*), possibly resulting from the proposed spinodal decomposition and subsequent mineralization process; and 3) the spectroscopic evidence of a Mg–CC phase containing more Mg in the discs than in the prism (*SI Appendix*, Fig. S2) are in very good agreement with this model. The compositional differences observed postcrystallization between young discs and mature prisms likely results from initial differences in the composition and/or from a different efficiency of the crystallization process. We note that this mechanism, along with a potential additional stabilization by hydration of the ACC might well be at play in the case of *P. margaritifera* biomineralization.

Conclusion

In conclusion, we have presented the quantitative characterization of amorphous calcium carbonate compounds in the shell of *P. margaritifera* by X-ray PDF techniques with submicrometric spatial resolution. Using PCA analysis of the PDF we show that distinct amorphous components are present in the periostracum as well as in young and older mineralizing units. Further analysis by RMC modeling unveils differences in the first coordination shell of ACC, with a notable contraction of the Ca–O atom pair distance in young discs. Combining these observations with SRS and EDX characterization, we can summarize these findings as a Mg-mediated ACC stabilization mechanism. Not only the presence of Mg fully explains the observed structural differences and appears more probable than the presence of several polyamorphous components, it is also in accord with recently published reports of the effects of Mg on the stabilization and crystallization of ACC.

This study sheds light on the nature of the amorphous calcium carbonate components and their role in the shell formation of *P. margaritifera* shell by establishing an experimental approach to obtain PDF data on partially crystalline systems. This opens the door for the study of other amorphous compounds in various biomineralizing systems like sea urchins or corals as well as expanding this approach to study technical materials such as energy-relevant materials.

Materials and Methods

***P. margaritifera* Specimens.** Juvenile specimens of *P. margaritifera* were grown in the 'Institut Français de Recherche pour l'Exploitation de la Mer' (IFREMER) hatchery facilities in Taravao-Vairao (Tahiti). They were cultivated under optimal growth conditions (pH = 8.2, T = 28 °C) and controlled sanitary environment to avoid contamination during the growth process. The samples used for PDF analysis were collected at an age of 48 d with a diameter of 7 mm, stored in a 70% ethanol solution and transferred to Marseille, France. The SRS and EDX samples were slightly older (3 mo, with a diameter of 10 mm) but produced in the exact same conditions. For the X-ray experiment, a small piece containing early stage mineralizing units was isolated and mounted on a metallic tip to feature a free-standing shell piece in the beam.

Coherent Raman Microscopy. Coherent Raman microscopy provides chemical sensitivity by targeting specific molecular transitions and observing the Raman shift of this transition with a spectral resolution of about 12 cm^{-1} (88) and a lateral resolution of about 350 nm. In this work, we employed the SRS imaging modality. In brief, two pulsed laser beams generated by a mode-locked laser (picoEmerald, APE, 80 MHz repetition rate), one laser at 1,032 nm (Stokes laser), and one other laser, tunable between 730 nm and 960 nm (pump laser), synchronized in time and space, are focused on the sample with a microscope objective (40×, numerical aperture [NA] 1.15, CFI Apo Lambda S LWD, Nikon). The wavelength difference between the two laser beams is tuned to the targeted molecular vibration. The signal is collected in transmission geometry with a long working distance in-air objective (40×, NA 0.6 LUCPLFLN, Olympus) and focusing on the detection module (APE SRS detection set), which comprises a photodiode and a lock-in amplification scheme. For the SRS data acquisition the beam intensity of the Stokes beam is modulated with an electrooptical modulator and

the intensity, transferred from the Stokes to the pump beam, is measured over an integration time of 100 ns (89). The sample was placed in a single-well 0.8-mm Secure-Seal spacer (Thermo Fisher), submerged in demineralized water, and covered with a coverslip on each side of the spacer. For the acquisition, the laser beams (75 mW power each) were scanned with a galvanometric scanner (6200 H, Cambridge Technology) over the sample with a step size of 400 nm laterally and 500 nm along the thickness direction. The total dwell time in every pixel was 80 μs and five scans were accumulated to produce the final map. Twelve wavenumbers were targeted between 1,057 and 1,105 cm^{-1} (see spectrum in Fig. 1*C*), including the C–O stretch ν1 mode (1,084 to 1,086 cm^{-1}) of calcite as well as an off-peak mode for ACC (1,073 to 1,081 cm^{-1}) and the Mg–CC range (1,092 to 1,093 cm^{-1}). For the analysis, three spectral ranges were defined to account for slight peak shifts due to varying composition of the sample, presented in Fig. 1*C* as blue (CC), red (ACC), and green (Mg–CC) ranges.

The amount of ACC and Mg–CC was compared to CC by calculating the symmetric difference maps for ACC and Mg–CC with respect to CC, as further described by Duboisset et al. (12). These maps correspond to the difference between the two intensity maps measured at different wavenumbers, normalized by the sum of the two intensity maps. The maps can be interpreted in the following way: A signal fully dominated by a CC contribution (resp., ACC or Mg–CC) would yield a value of +1 (resp,. −1), while a value of 0 would indicate equivalent contributions of CC and ACC/Mg–CC (only if the peak widths are similar). This approach allows one to extract a qualitative phase content without the need to deconvolute the spectra and the unknown respective peak widths of the ACC and CC and Mg–CC phases.

Micro-Raman Spectroscopy. Raman spectroscopy, although less sensitive than SRS (90), allows the increase of the spectral resolution to follow more subtle changes in the peak position. Raman measurements were carried out on a LabRAM HR 800 instrument (Horiba) equipped with a 632.8-nm laser and a peltier-cooled charge-coupled device camera. Together with a 1,200 lines/mm grating and the 800-mm spectrometer path, this gave a spectral resolution of ∼0.6 cm^{-1}. The laser was focused onto the sample with an in-air objective (100×, NA 0.9, MPLAN, Olympus). A 200-μm confocal pinhole on the spectrometer beampath defines the spatial resolution to ∼2 μm. The sample area of 40 × 40 μm was scanned with a 1-μm step size to ensure slight oversampling with an exposure time of 25 s and two repetitions per point. The spectral window of the spectrometer was selected as 650 to 1,250 cm^{-1}. After correction for the CCD dark noise, the baseline was fitted as a fourth order polynomial model and subtracted from the data. The C–O stretch ν1 region (1,064 to 1,107 cm^{-1}) was fitted with three Lorentzian peak model and a linear background. The three peaks constituted the ACC, CC, and Mg–CC contribution. The ACC peak width and position were restrained to 20 to 60 cm^{-1} and 1,070 to 1,082 cm^{-1}, respectively. The CC peak position was fixed at the calcite reference position (65) (1,085.71 cm^{-1}) and the width restrained to 4 to 9 cm^{-1}. The Mg–CC peak width and position were restrained to 4 to 10 cm^{-1} and 1,086.7 to 1,096 cm^{-1}, respectively. All peaks were enforced to be positive. The Mg content of the Mg–CC phase was estimated from the peak shift of the Mg–CC position with the linear relation 1,085.71 + 0.256 *x*, where *x* is the Mg content in the $Mg_xCa_{(1-x)}CO_3$ solid solution, expressed in mol% (65). The results are presented in *SI Appendix*, Fig. 2 and the full fit results are presented in *SI Appendix*, Fig. 3. The average Mg content was compared for the young and mature prism and significance tested with a two-sample *t* test and a significance level of 0.005.

X-Ray Data Acquisition. The X-ray experiments were carried out at the ID15A (66) beamline at the European Synchrotron Radiation Facility (ESRF, pre Extremely Brilliant Source upgrade). A monochromatic beam with an energy of 60 keV (0.206 Å) and an energy bandwidth of 0.25% was selected with a LN_2 cooled Si (111) Laue monochromator. The X-rays were focused to a spot of 300 × 500 nm full width at half maximum with a dynamically bent multilayer Kirkpatrick-Baez mirror system. The sample had a thickness of ∼1 μm and was illuminated in a transmission geometry. The forward scattered photons were collected using a Dectris Pilatus3 X CdTe 2M detector, placed 215 mm downstream of the sample, giving access to a scattering vector *q* range of 1 to 22 $Å^{-1}$. A beam stop placed directly in front of the detector was used to block the direct beam. The fluorescence photons were detected with a Hitachi Vortex EM XRF detector. In order to minimize air scattering from the transmitted direct beam, the air path was reduced by placing a helium-filled flight tube between the sample and the beam stop.

For the data acquisition, as the investigated early-stage mineralization unit (disc) already showed some crystallization, the sample was rotated from −15° to 15° around ω and data were collected in 1° increments with 20-s exposure time at each point. Two line scans across an early stage mineralization unit (disc) were carried out with a step size of 1 μm each. The horizontal and vertical lines covered 50 and 38 μm, respectively. At the beginning of each line scan a background was acquired with the same scan parameters by removing the sample from the X-ray beam.

SEM and SEM-EDX Data Acquisition. The SEM micrograph shown in Fig. 1*B* was acquired with a Phenom X Pro. The samples were mounted with carbon tape and the instrument was operated in low-vacuum mode to reduce sample charging. The acceleration voltage was set to 15 kV and the backscattered electrons were used as the imaging contrast. The SEM-EDX data shown in Fig. 1*F* were acquired on a JSM-7900F (Jeol) with an annular flat-quad detector XFlash 5060F (Bruker). Samples were fixed on carbon tape and sputtered with a thin layer of C. Data were acquired at 6 kV acceleration voltage in high-vacuum mode with a pixel dwell time of 32 μs and 764 repetitions.

Data Processing. The following section presents an overview of the data reduction steps from the 2D scattering images to the calculation of the PDF (*SI Appendix*, Fig. 4). The X-ray data were first normalized to the incident beam intensity and the sample data were corrected for the 2D background scattering. The (q,χ) intensity distributions were azimuthally regrouped using pyFAI (91) with custom-written python scripts. From the full rocking curve data at every spatial position, the median was calculated first along the rocking curve direction and then along the azimuthal direction to separate the diffuse scattering signal from possible crystalline contributions (*SI Appendix*, Fig. 4*B*). The rationale behind this approach is that a reflection from the crystalline part of the sample is more localized in reciprocal space (i.e., tails off fast when not in Bragg condition) compared to the isotropic and diffuse signal from the nonperiodic part of the sample. Therefore, the total scattering intensity from the sample was sorted along both ω and χ and a low-pass filter was applied to obtain an azimuthally integrated *I(q)* virtually rid of contributions from crystalline CC. The *I(q)* scattering curves (as shown in Fig. 3*A*) were binned in constant steps of *q*, with $\boldsymbol{q}$ the wavevector transfer defined as:

$$q = \frac{4\pi \sin\theta}{\lambda}, \qquad [1]$$

where 2θ is the scattering angle and λ the X-ray wavelength. The following section gives a brief overview over the PDF formalism used, based on Peterson et al. (92). The scattered intensity *I(q)* can be related to a set of atomic coordinates through the Debye scattering equation and includes effects of thermal atomic displacement by introducing the Debye-Waller term $\sigma_{\nu\mu}$.

$$I(q) = \sum_{\nu\mu} b_{coh,\nu} b_{coh,\mu} \frac{\sin\left(q r_{\nu\mu}\right)}{q r_{\nu\mu}} \exp\left(\frac{-\sigma_{\nu\mu}^2 q^2}{2}\right), \qquad [2]$$

where $b_{coh,\nu}$ is the coherent scattering length of atom ν, and $r_{\nu\mu} = \left|r_\nu - r_\mu\right|$ is the interatomic pairwise vector of atoms ν and μ. The commonly used structure function *S(q)* is introduced to normalize *I(q)* and correct it by the Laue diffuse scattering term:

$$S(q) = \frac{I(q)}{N\langle b_{coh}\rangle^2} - \frac{\langle b_{tot}^2\rangle - \langle b_{coh}\rangle^2}{\langle b_{coh}\rangle^2}, \qquad [3]$$

where *N* is the number of atoms illuminated in the sample, $\langle b_{tot}^2\rangle = \langle\sigma_{tot}\rangle/4\pi$ is the average total scattering power of the system, σ_{tot} is the total cross-section, and $\langle b_{coh}\rangle^2$ is the average coherent scattering power of all atoms in the sample. This expression can be related to the commonly employed reduced total scattering structure function *F(q)*

$$F(q) = q[S(q) - 1]. \qquad [4]$$

This description takes the *q* dependence of X-ray scattering factors into account and enhances the weight of the scattering at high *q*. From *F(q)*, the PDF was calculated as *G(r)*

$$G(r) = \frac{2}{\pi}\int_0^\infty F(q)\sin(qr)dq. \qquad [5]$$

The PDF was then scaled to $D(r)$ for RMC refinements

$$D(r) = \langle b \rangle^2 G(r). \quad [6]$$

The reader is referred to Keen et al. (93) for a further discussion of the different scaling terms. In order to enable non-negative matrix factorization, the data need to be scaled to zero mean and unit variance, yielding $D'(r)$

$$D'(r) = \frac{(D(r) - mean(D(r)))}{standard\ deviation(D(r))}. \quad [7]$$

To ensure positivity for the non-negative matrix factorization, the $G'(r)$ function (69) was obtained as:

$$G'(r) = \frac{D'(r)}{4\pi\rho_0 r} + 1, \quad [8]$$

where ρ_0 is the average number density of the material and the limiting values are:

$$\begin{aligned} G'(r < r^0) &= 0 \\ G'(r \to \infty) &= 1. \end{aligned} \quad [9]$$

The q range from 1 to 18 $Å^{-1}$ was used for the initial $G(r)$ calculation in the pdfgetx3 code (94). The effect of the q_{max} cutoff was investigated in more detail and the results are presented in *SI Appendix*, Fig. 8. The monohydrocalcite stoichiometry ($CaCO_3$*H_2O) was used to estimate the density (mass $\rho = 2.38$ g/cm^3) for the calculation of the weighted total scattering factor $S(q)$, $F(q)$, and $D(r)$.

To minimize propagating systematic noise introduced by the data reduction (azimuthally regrouping and filtering) to the diffraction data, the $F(q)$ data were fitted with splines prior to Fourier transform. The rationale of the approach is that correctly weighted splines can eliminate outliers instead of redistributing their intensity through smoothing (51). To check for bias in the PDF data thus obtained, the analysis was repeated on two more iterations of $F(q)$ spline fitting: one closely reproducing the raw $F(q)$ and one with a reduced number of knots (i.e., more outliers rejected). Subsequent fittings and analysis on the three variants of the same data confirmed the robustness of the approach. A comparison of the procedure can be seen in *SI Appendix*, Fig. 3.

Data Analysis (PCA and RMC). The goal of multivariate PCA analysis of the PDF data (56, 57) is to represent the full dataset as a series of linear combinations of a small number of significant components, their relative weights changing between the points of the line scan across the early stage mineralization unit. For multivariate analysis, the series of $G'(r)$ data were used (93) to ensure positiveness of the matrix formed by data points along the line scans. Non-negative matrix factorization of the preshaped data were done using the python-scikit-learn package (95). From a random initial guess the non-negative matrix factorization algorithm calculates profile and weight of a specified number of components in order to minimize the difference between their linear combination and the experimental $G'(r)$. The number of significant components was estimated by eigenvalue analysis of the data matrix, whereby three components were found to account for >96% of data variance across the sample line scan.

Atomistic structural models of the amorphous calcium carbonate mixture were obtained through reverse Monte Carlo fits of the $D(r)$ PDF data, using the software RMC profile (58). The initial structural model is an hexagonal monohydrocalcite cell expanded to a $6 \times 6 \times 6$ supercell. To account for the presence of proteins, an additional C–O group was added per each $CaCO_3$ molecule. It was decided to not include Mg atoms as an additional atomic species as the scattering length differences between Mg and Ca make the distinction difficult as the Mg pairs are largely "invisible" next to their Ca counterparts. A summary is given in *SI Appendix*, Table 4. Reports in the literature underline the difficulty of refining Mg atom pairs next to Ca atom pairs with X-ray methods (96). Furthermore, our own simulations where 5% Mg inclusion was tested in our RMC model show neglibile impact of the Mg presence on the atom pair distance (*SI Appendix*, Fig. 9*A*) and a general increase of the residual error during the refinement (*SI Appendix*, Fig. 9*B*).

The density of the supercell was chosen as 2.38 g/cm^3, corresponding to the monohydrocalcite density. We further used the u-curve approach (*SI Appendix*, Fig. 10), outlined by Gereben and Pusztai (97) and employed also by Goodwin et al. for the case of ACC (48), to estimate density and obtained a minimum value of ~2.4 g/cm^3, matching well with the chosen density. The u curve was run on horizontal point #30 with a fixed scaling term. Distance restraints between nearest-neighbor atom pairs were imposed in order to preserve physical cation–anion distances, given in *SI Appendix*, Table 5. The fitting range was limited to 10 Å due to the absence of long-range order in ACC. Atomistic configurations corresponding to the best fit for each scan point were analyzed using python scripts after removing the protein C–O from the fitted atomic configuration. The atom pair distances and coordination numbers for the Ca–O (0 to 2.8 Å), Ca–C (3 to 3.5 Å), and Ca–Ca (0 to 4 Å) were extracted from the fitted data. The threshold values were chosen to include the first full coordination shell around the central Ca atom. The SE was estimated for each bond type and the error bars for the 99.7% confidence interval are included in Fig. 5. A further breakdown of the errors in each subcell is presented in *SI Appendix*, Fig. 11.

Data, Materials, and Software Availability. All study data are included in the article and/or supporting information.

ACKNOWLEDGMENTS. We acknowledge the ESRF, Grenoble, France for supplying beam time for the experiments and the Partnership for Soft Condensed Matter for support during the preparation of the experiment. We acknowledge the help of Ifremer Taravao for giving access to the shell samples and Gavin Vaughan (ESRF) for helpful discussions on the PDF data processing. This work received funding from the European Research Council (European Union's Horizon H2020 research and innovation program grant agreement No. 724881). This study is set within the framework of the Laboratoire d'Excellence (LabEx) TULIP (ANR-10-LABX-41).

Author affiliations: [a]Aix-Marseille Univ, CNRS, Centrale Marseille, Institut Fresnel, Marseille, F-13013 France; [b]ESRF – The European Synchrotron, Grenoble Cedex, F-38043 France; [c]Ifremer, IRD, Institut Louis-Malardé, Univ Polynésie française, EIO, F-98719 Taravao Tahiti, Polynésie française, France; [d]IHPE, University Montpellier, CNRS, IFREMER, University Perpignan Via Domitia, Montpellier, France; [e]Geosciences Paris Saclay, Université Paris-Saclay, CNRS, 91405 Orsay, France; and [f]Aix-Marseille Univ, CNRS, CINaM, Campus Luminy, Marseille, France

1. H. A. Lowenstam, S. Weiner, *On Biomineralization* (Oxford University Press, 1989).
2. Y. Dauphin, The nanostructural unity of Mollusc shells. *Mineral. Mag.* **72**, 243–246 (2008).
3. S. E. Wolf *et al.*, Single nanogranules preserve intracrystalline amorphicity in biominerals. *Key Eng. Mater.* **672**, 47–59 (2016).
4. S. E. Wolf *et al.*, Nonclassical crystallization in vivo et in vitro (I): Process-structure-property relationships of nanogranular biominerals. *J. Struct. Biol.* **196**, 244–259 (2016).
5. P. U. P. A. Gilbert *et al.*, Biomineralization by particle attachment in early animals. *Proc. Natl. Acad. Sci. U.S.A.* **116**, 17659–17665 (2019).
6. F. Bouville *et al.*, Strong, tough and stiff bioinspired ceramics from brittle constituents. *Nat. Mater.* **13**, 508–514 (2014).
7. H. Le Ferrand, F. Bouville, T. P. Niebel, A. R. Studart, Magnetically assisted slip casting of bioinspired heterogeneous composites. *Nat. Mater.* **14**, 1172–1179 (2015).
8. T. de Garidel-Thoron, Y. Rosenthal, F. Bassinot, L. Beaufort, Stable sea surface temperatures in the western Pacific warm pool over the past 1.75 million years. *Nature* **433**, 294–298 (2005).
9. J. Seto *et al.*, Structure-property relationships of a biological mesocrystal in the adult sea urchin spine. *Proc. Natl. Acad. Sci. U.S.A.* **109**, 3699–3704 (2012).
10. Y. U. T. Gong *et al.*, Phase transitions in biogenic amorphous calcium carbonate. *Proc. Natl. Acad. Sci. U.S.A.* **109**, 6088–6093 (2012).
11. Y. Politi *et al.*, Transformation mechanism of amorphous calcium carbonate into calcite in the sea urchin larval spicule. *Proc. Natl. Acad. Sci. U.S.A.* **105**, 17362–17366 (2008).
12. J. Duboisset *et al.*, Amorphous-to-crystal transition in the layer-by-layer growth of bivalve shell prisms. *Acta Biomater.* **142**, 194–207 (2022).
13. I. M. Weiss, N. Tuross, L. Addadi, S. Weiner, Mollusc larval shell formation: Amorphous calcium carbonate is a precursor phase for aragonite. *J. Exp. Zool.* **293**, 478–491 (2002).
14. N. Nassif *et al.*, Amorphous layer around aragonite platelets in nacre. *Proc. Natl. Acad. Sci. U.S.A.* **102**, 12653–12655 (2005).
15. B. Hasse, H. Ehrenberg, J. C. Marxen, W. Becker, M. Epple, Calcium carbonate modifications in the mineralized shell of the freshwater snail Biomphalaria glabrata. *Chemistry* **6**, 3679–3685 (2000).
16. F. Nudelman, H. H. Chen, H. A. Goldberg, S. Weiner, L. Addadi, Spiers Memorial Lecture. Lessons from biomineralization: Comparing the growth strategies of mollusc shell prismatic and nacreous layers in Atrina rigida. *Faraday Discuss.* **136**, 9–25, discussion 107–123 (2007).
17. A. Baronnet, J. P. Cuif, Y. Dauphin, B. Farre, J. Nouet, Crystallization of biogenic Ca-carbonate within organo-mineral micro-domains. Structure of the calcite prisms of the Pelecypod Pinctada margaritifera (Mollusca) at the submicron to nanometre ranges. *Mineral. Mag.* **72**, 617–626 (2008).
18. E. Macías-Sánchez, M. G. Willinger, C. M. Pina, A. G. Checa, Transformation of ACC into aragonite and the origin of the nanogranular structure of nacre. *Sci. Rep.* **7**, 12728 (2017).
19. A. Becker *et al.*, Structural characterisation of X-ray amorphous calcium carbonate (ACC) in sternal deposits of the crustacea Porcellio scaber. *Dalton Trans.*551–555 (2003).
20. R. J. Reeder *et al.*, Characterization of structure in biogenic amorphous calcium carbonate: Pair distribution function and nuclear magnetic resonance studies of lobster gastrolith. *Cryst. Growth Des.* **13**, 1905–1914 (2013).

21. S. Raz, P. C. Hamilton, F. H. Wilt, S. Weiner, L. Addadi, The transient phase of amorphous calcium carbonate in sea urchin larval spicules: The involvement of proteins and magnesium ions in its formation and stabilization. *Adv. Funct. Mater.* **13**, 480–486 (2003).
22. E. M. Pouget *et al.*, The initial stages of template-controlled $CaCO_3$ formation revealed by cryo-TEM. *Science* **323**, 1455–1458 (2009).
23. F. Nudelman, E. Sonmezler, P. H. H. Bomans, G. de With, N. A. J. M. Sommerdijk, Stabilization of amorphous calcium carbonate by controlling its particle size. *Nanoscale* **2**, 2436–2439 (2010).
24. Y. Politi *et al.*, Role of magnesium ion in the stabilization of biogenic amorphous calcium carbonate: A structure—function investigation. *Chem. Mater.* **22**, 161–166 (2010).
25. L. Xiang *et al.*, Amorphous calcium carbonate precipitation by cellular biomineralization in mantle cell cultures of Pinctada fucata. *PLoS One* **9**, e113150 (2014).
26. J. H. E. Cartwright, A. G. Checa, J. D. Gale, D. Gebauer, C. I. Sainz-Díaz, Calcium carbonate polyamorphism and its role in biomineralization: How many amorphous calcium carbonates are there? *Angew. Chem. Int. Ed. Engl.* **51**, 11960–11970 (2012).
27. A. Fernandez-Martinez, B. Kalkan, S. M. Clark, G. A. Waychunas, Pressure-induced polyamorphism and formation of 'aragonitic' amorphous calcium carbonate. *Angew. Chem. Int. Ed. Engl.* **52**, 8354–8357 (2013).
28. D. Gebauer *et al.*, Proto-calcite and proto-vaterite in amorphous calcium carbonates. *Angew. Chem. Int. Ed. Engl.* **49**, 8889–8891 (2010).
29. M. Farhadi-Khouzani, D. M. Chevrier, P. Zhang, N. Hedin, D. Gebauer, Water as the key to proto-aragonite amorphous $CaCO_3$. *Angew. Chem. Int. Ed. Engl.* **55**, 8117–8120 (2016).
30. D. Gebauer, H. Cölfen, A. Verch, M. Antonietti, The multiple roles of additives in $CaCO_3$ crystallization: A quantitative case study. *Adv. Mater.* **21**, 435–439 (2009).
31. D. Gebauer, A. Völkel, H. Cölfen, Stable prenucleation calcium carbonate clusters. *Science* **322**, 1819–1822 (2008).
32. T. Mass *et al.*, Amorphous calcium carbonate particles form coral skeletons. *Proc. Natl. Acad. Sci. U.S.A.* **114**, E7670–E7678 (2017).
33. M. Albéric *et al.*, Interplay between calcite, amorphous calcium carbonate, and intracrystalline organics in sea urchin skeletal elements. *Cryst. Growth Des.* **18**, 2189–2201 (2018).
34. M. Albéric *et al.*, Growth and regrowth of adult sea urchin spines involve hydrated and anhydrous amorphous calcium carbonate precursors. *J. Struct. Biol. X* **1**, 100004 (2019).
35. R. T. DeVol *et al.*, Nanoscale transforming mineral phases in fresh nacre. *J. Am. Chem. Soc.* **137**, 13325–13333 (2015).
36. S. Amarie *et al.*, Nano-FTIR chemical mapping of minerals in biological materials. *Beilstein J. Nanotechnol.* **3**, 312–323 (2012).
37. A. Masic, J. C. Weaver, Large area sub-micron chemical imaging of magnesium in sea urchin teeth. *J. Struct. Biol.* **189**, 269–275 (2015).
38. W. J. E. M. Habraken *et al.*, Layered growth of crayfish gastrolith: About the stability of amorphous calcium carbonate and role of additives. *J. Struct. Biol.* **189**, 28–36 (2015).
39. H. C. Lichtenegger *et al.*, Zinc and mechanical prowess in the jaws of Nereis, a marine worm. *Proc. Natl. Acad. Sci. U.S.A.* **100**, 9144–9149 (2003).
40. B. H. Frazer, M. Girasole, L. M. Wiese, T. Franz, G. De Stasio, Spectromicroscope for the PHotoelectron Imaging of Nanostructures with X-rays (SPHINX): performance in biology, medicine and geology. *Ultramicroscopy* **99**, 87–94 (2004).
41. B. H. Frazer, B. Gilbert, B. R. Sonderegger, G. De Stasio, The probing depth of total electron yield in the sub-keV range: TEY-XAS and X-PEEM. *Surf. Sci.* **537**, 161–167 (2003).
42. P. Tack *et al.*, Application toward confocal full-field microscopic X-ray absorption near edge structure spectroscopy. *Anal. Chem.* **89**, 2123–2130 (2017).
43. A. M. Maiden, G. R. Morrison, B. Kaulich, A. Gianoncelli, J. M. Rodenburg, Soft X-ray spectromicroscopy using ptychography with randomly phased illumination. *Nat. Commun.* **4**, 1669 (2013).
44. M. Beckers *et al.*, Chemical contrast in soft x-ray ptychography. *Phys. Rev. Lett.* **107**, 208101 (2011).
45. Z. Gao *et al.*, Sparse ab initio x-ray transmission spectrotomography for nanoscopic compositional analysis of functional materials. *Sci. Adv.* **7**, eabf6971 (2021).
46. X. Zhu *et al.*, Measuring spectroscopy and magnetism of extracted and intracellular magnetosomes using soft X-ray ptychography. *Proc. Natl. Acad. Sci. U.S.A.* **113**, E8219–E8227 (2016).
47. F. M. Michel *et al.*, Structural characteristics of synthetic amorphous calcium carbonate. *Chem. Mater.* **20**, 4720–4728 (2008).
48. A. L. Goodwin *et al.*, Nanoporous structure and medium-range order in synthetic amorphous calcium carbonate. *Chem. Mater.* **22**, 3197–3205 (2010).
49. S. M. Clark *et al.*, The nano- and meso-scale structure of amorphous calcium carbonate. *Sci. Rep.* **12**, 6870 (2022).
50. L. B. Skinner *et al.*, Molten uranium dioxide structure and dynamics. *Science* **346**, 984–987 (2014).
51. L. B. Skinner *et al.*, Joint diffraction and modeling approach to the structure of liquid alumina. *Phys. Rev. B Condens. Matter Mater. Phys.* **87**, 024201 (2013).
52. R. J. Reeder, F. M. Michel, "Application of total X-ray scattering methods and pair distribution function analysis for study of structure of biominerals" in *Methods in Enzymology*. James J. De Yoreo, Ed. (Elsevier, 2013), pp. 477–500.
53. X. Hong *et al.*, High-energy X-ray focusing and applications to pair distribution function investigation of Pt and Au nanoparticles at high pressures. *Sci. Rep.* **6**, 21434 (2016).
54. A.-C. Dippel *et al.*, Local atomic structure of thin and ultrathin films *via* rapid high-energy X-ray total scattering at grazing incidence. *IUCrJ* **6**, 290–298 (2019).
55. S. D. M. Jacques *et al.*, Pair distribution function computed tomography. *Nat. Commun.* **4**, 2536 (2013).
56. K. W. Chapman, S. H. Lapidus, P. J. Chupas, Applications of principal component analysis to pair distribution function data. *J. Appl. Cryst.* **48**, 1619–1626 (2015).
57. H. S. Geddes, H. Blade, J. F. McCabe, L. P. Hughes, A. L. Goodwin, Structural characterisation of amorphous solid dispersions via metropolis matrix factorisation of pair distribution function data. *Chem. Commun. (Camb.)* **55**, 13346–13349 (2019).
58. M. G. Tucker, D. A. Keen, M. T. Dove, A. L. Goodwin, Q. Hui, RMCProfile: Reverse Monte Carlo for polycrystalline materials. *J. Phys. Condens. Matter* **19**, 335218 (2007).
59. J.-P. Cuif *et al.*, Evidence of a biological control over origin, growth and end of the calcite prisms in the shells of *Pinctada margaritifera* (Pelecypod, Pterioidea). *Minerals (Basel)* **4**, 815–834 (2014).
60. A. G. Checa, E. Macías-Sánchez, E. M. Harper, J. H. E. Cartwright, Organic membranes determine the pattern of the columnar prismatic layer of mollusc shells. *Proc. Biol. Sci.* **283**, 20160032 (2016).
61. O. B. A. Agbaje, I. Ben Shir, D. B. Zax, A. Schmidt, D. E. Jacob, Biomacromolecules within bivalve shells: Is chitin abundant? *Acta Biomater.* **80**, 176–187 (2018).
62. B. Marie *et al.*, Different secretory repertoires control the biomineralization processes of prism and nacre deposition of the pearl oyster shell. *Proc. Natl. Acad. Sci. U.S.A.* **109**, 20986–20991 (2012).
63. G. Nehrke, J. Nouet, Confocal Raman microscope mapping as a tool to describe different mineral and organic phases at high spatial resolution within marine biogenic carbonates: Case study on *Nerita undata* (Gastropoda, Neritopsina). *Biogeosciences* **8**, 3761–3769 (2011).
64. L. Addadi, S. Raz, S. Weiner, Taking advantage of disorder: Amorphous calcium carbonate and its roles in biomineralization. *Adv. Mater.* **15**, 959–970 (2003).
65. J. Perrin *et al.*, Raman characterization of synthetic magnesian calcites. *Am. Mineral.* **101**, 2525–2538 (2016).
66. G. B. M. Vaughan *et al.*, ID15A at the ESRF–A beamline for high speed operando X-ray diffraction, diffraction tomography and total scattering. *J. Synchrotron Radiat.* **27**, 515–528 (2020).
67. M. Ruat, C. Ponchut, Characterization of a pixelated CdTe X-ray detector using the timepix photon-counting readout chip. *IEEE Trans. Nucl. Sci.* **59**, 2392–2401 (2012).
68. P. Zambon *et al.*, Spectral response characterization of CdTe sensors of different pixel size with the IBEX ASIC. *Nucl. Instrum. Methods Phys. Res. A* **892**, 106–113 (2018).
69. M. P. Prange, S. T. Mergelsberg, S. N. Kerisit, Ab initio molecular dynamics simulations of amorphous calcium carbonate: Interpretation of pair distribution function and X-ray absorption spectroscopy data. *Cryst. Growth Des.* **21**, 2212–2221 (2021).
70. G. Yamamoto, A. Kyono, S. Okada, Temperature dependence of amorphous magnesium carbonate structure studied by PDF and XAFS analyses. *Sci. Rep.* **11**, 22876 (2021).
71. C. E. White, N. J. Henson, L. L. Daemen, M. Hartl, K. Page, Uncovering the true atomic structure of disordered materials: The structure of a hydrated amorphous magnesium carbonate ($MgCO_3 \cdot 3D_2O$). *Chem. Mater.* **26**, 2693–2702 (2014).
72. I. Polishchuk *et al.*, Coherently aligned nanoparticles within a biogenic single crystal: A biological prestressing strategy. *Science* **358**, 1294–1298 (2017).
73. E. Seknazi *et al.*, From spinodal decomposition to alternating layered structure within single crystals of biogenic magnesium calcite. *Nat. Commun.* **10**, 4559 (2019).
74. N. Bianco-Stein *et al.*, High-Mg calcite nanoparticles within a low-Mg calcite matrix: A widespread phenomenon in biomineralization. *Proc. Natl. Acad. Sci. U.S.A.* **119**, e2120177119 (2022).
75. A. V. Radha *et al.*, Energetic and structural studies of amorphous Ca1−xMgxCO3·nH2O (0⩽x⩽1). *Geochim. Cosmochim. Acta* **90**, 83–95 (2012).
76. Z. Liu *et al.*, Shape-preserving amorphous-to-crystalline transformation of $CaCO_3$ revealed by in situ TEM. *Proc. Natl. Acad. Sci. U.S.A.* **117**, 3397–3404 (2020).
77. M. Albéric *et al.*, The crystallization of amorphous calcium carbonate is kinetically governed by ion impurities and water. *Adv. Sci. (Weinh.)* **5**, 1701000 (2018).
78. E. Zolotoyabko *et al.*, Differences between bond lengths in biogenic and geological calcite. *Cryst. Growth Des.* **10**, 8 (2010).
79. H. Effenberger, K. Mereiter, J. Zemann, Crystal structure refinements of magnesite, calcite, rhodochrosite, siderite, smithonite, and dolomite, with discussion of some aspects of stereochemistry of calcite type carbonates. *Z. Kristallogr.* **156**, 10 (1981).
80. J. Ihli *et al.*, Dehydration and crystallization of amorphous calcium carbonate in solution and in air. *Nat. Commun.* **5**, 3169 (2014).
81. M. P. Schmidt, A. J. Ilott, B. L. Phillips, R. J. Reeder, Structural Changes upon Dehydration of Amorphous Calcium Carbonate. *Cryst. Growth Des.* **14**, 938–951 (2014).
82. M. Saharay, A. O. Yazaydin, R. J. Kirkpatrick, Dehydration-induced amorphous phases of calcium carbonate. *J. Phys. Chem. B* **117**, 3328–3336 (2013).
83. A. V. Radha, T. Z. Forbes, C. E. Killian, P. U. P. A. Gilbert, A. Navrotsky, Transformation and crystallization energetics of synthetic and biogenic amorphous calcium carbonate. *Proc. Natl. Acad. Sci. U.S.A.* **107**, 16438–16443 (2010).
84. M. P. Asta *et al.*, Nanoscale ion dynamics control on amorphous calcium carbonate crystallization: Precise control of calcite crystal sizes. *J. Phys. Chem. C* **124**, 25645–25656 (2020).
85. K. Kahil, S. Weiner, L. Addadi, A. Gal, Ion pathways in biomineralization: Perspectives on uptake, transport, and deposition of calcium, carbonate, and phosphate. *J. Am. Chem. Soc.* **143**, 21100–21112 (2021).
86. Z. Zou *et al.*, Additives control the stability of amorphous calcium carbonate via two different mechanisms: Surface adsorption versus bulk incorporation. *Adv. Funct. Mater.* **30**, 2000003 (2020).
87. S. T. Mergelsberg *et al.*, Metastable solubility and local structure of amorphous calcium carbonate (ACC). *Geochim. Cosmochim. Acta* **289**, 196–206 (2020).
88. J.-X. Cheng, X. S. Xie, *Coherent Raman Scattering Microscopy* (CRC Press, 2018).
89. C. Zhang, J.-X. Cheng, Perspective: Coherent Raman scattering microscopy, the future is bright. *APL Photonics* **3**, 090901 (2018).
90. G. I. Petrov *et al.*, Comparison of coherent and spontaneous Raman microspectroscopies for noninvasive detection of single bacterial endospores. *Proc. Natl. Acad. Sci. U.S.A.* **104**, 7776–7779 (2007).
91. G. Ashiotis *et al.*, The fast azimuthal integration Python library: *PyFAI*. *J. Appl. Cryst.* **48**, 510–519 (2015).
92. P. F. Peterson, D. Olds, M. T. McDonnell, K. Page, Illustrated formalisms for total scattering data: A guide for new practitioners. *J. Appl. Cryst.* **54**, 317–332 (2021).
93. D. A. Keen, A comparison of various commonly used correlation functions for describing total scattering. *J. Appl. Cryst.* **34**, 172–177 (2001).
94. P. Juhás, T. Davis, C. L. Farrow, S. J. L. Billinge, PDFgetX3: A rapid and highly automatable program for processing powder diffraction data into total scattering pair distribution functions. *J. Appl. Cryst.* **46**, 560–566 (2013).
95. F. Pedregosa, *et al.*, Scikit-learn: Machine learning in python. arXiv [Preprint] (2011).
96. G. Cobourne *et al.*, Neutron and X-ray diffraction and empirical potential structure refinement modelling of magnesium stabilised amorphous calcium carbonate. *J. Non-Cryst. Solids* **401**, 154–158 (2014).
97. O. Gereben, L. Pusztai, The determination of the microscopic density in liquids and other disordered materials using reverse Monte Carlo simulation. *Phys. Chem. Liquids* **31**, 159–167 (1996).